RESEARCH ARTICLE

Figures and figure supplements

A tension-adhesion feedback loop in plant epidermis

Stéphane Verger *et al*

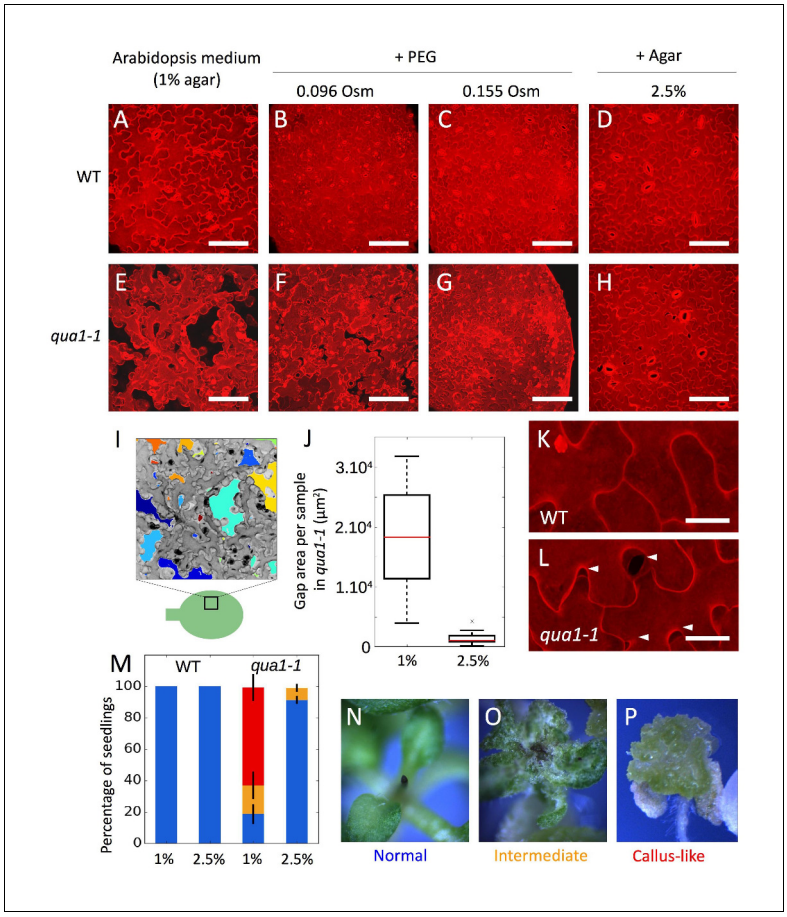

Figure 1. Adhesion defects in *qua1* mutant scale to the water potential of the growth medium. (**A–H**) Z-projections (maximal intensity) of confocal stacks from representative (12 samples observed in three biological replicates for each condition), propidium iodide stained, five days old cotyledons, showing the effect of the decreased medium water potential in the wild type (**A–D**) and the *qua1-1* mutant (**E–H**). A and E are standard growth condition. B-D and F-H are growth conditions with decreased water potential. B, F and C, G water potential is deceased with PEG, which increases the osmolarity of the medium of 96 mOsm (**B, F**) and 155 mOsm (**C, G**). In D and H water potential is decreased by increasing the agar concentration in the medium to 2.5%. (**I**) Representation of the semi automated image analysis process used to detect and quantify the area of gaps per sample shown in I (method further described in the material and method section and ***Figure 1—figure supplement 4***). The upper part: Z-projections (maximal intensity) of a confocal stack in grayscale color and inverted pixel intensity corresponding to panel E. Cell separations are identified and labeled in multiple colors for visualization. The bottom part: schematic representation of a cotyledon and the relative position where Z-stacks were taken (square). (**J**) Box plot of the quantification of the total area of cell separation per image analyzed, in 1% and 2.5% agar growth conditions, and corresponding to the comparison of the panels E and H (12 samples quantified in three biological replicates for each condition, Welch's *t*-test p-value=0.0004). (**K–L**) Close-up from (**D**) and (**H**) respectively, showing the cell separations preferentially happening at the lobe-neck junction (Arrow heads), in the *qua1-1* mutant (**L**). (**M**) Phenotype of the shoot apex in the wild type and *qua1-1* mutant, grown on 1% and 2.5% agar medium (210 seedlings in three biological repetitions per condition, error bars represent the standard deviation over the three biological replicates). Color code is explained in panels N-P: normal stem and meristem (Blue, **N**), a callus-like apex (Red, **P**) or an intermediate phenotype (Orange, **O**). (**N–P**) Stereo microscope images of representative phenotypes as used for the quantifications shown in M. Scale bars (**A–H**), 100 µm. Scale bars (**K,L**), 20 µm.

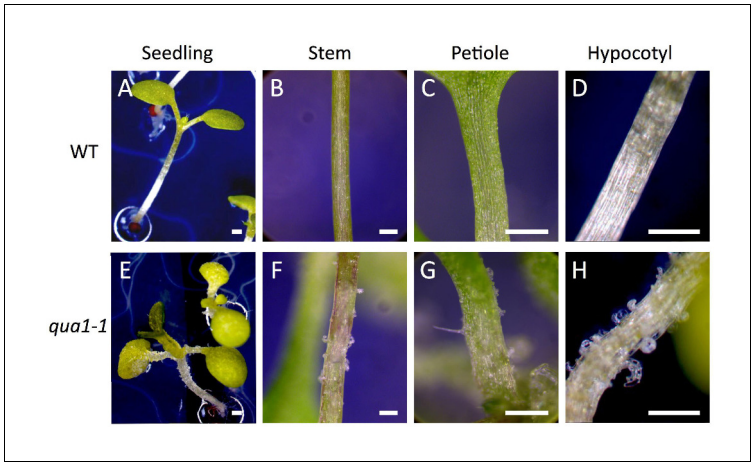

Figure 1—figure supplement 1. Widespread cell adhesion defects in the *qua1-1* mutant. (**A–H**) Stereomicroscope images of wild type (**A–D**) and *qua1-1* mutant (**E–H**), seedling (**A, E**), inflorescence stem (**B, F**), petiole (**C, G**), and hypocotyl (**D, H**). Scale bars, 400 μm.

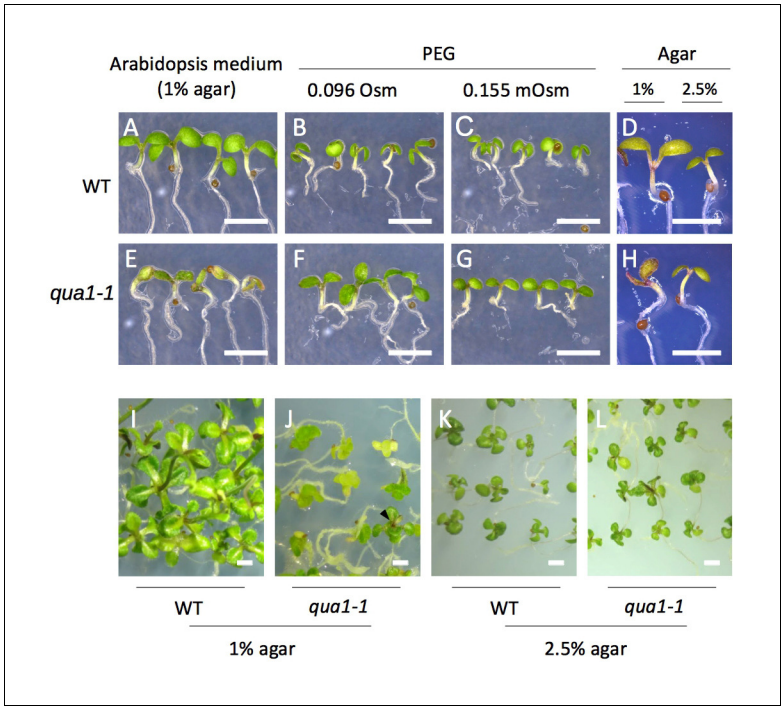

Figure 1—figure supplement 2. Seedling phenotypes in *qua1* mutant depend on the water potential of the growth medium. (**A–H**) Stereo-microscope images of 5-day old seedlings. The growth conditions are similar to ***Figure 1A–H***. (**I–L**) stereo microscope images of 4-week old wild-type (**I, K**) and *qua1-1* mutant (**J, L**) seedlings grown on NPA containing medium. Arrowhead in panel J points to a 'normal' seedling, the other seedlings exhibiting a callus-like (see ***Figure 1M–P***) The growth conditions are similar to ***Figure 1M–P***. Scale bars, 2 mm.

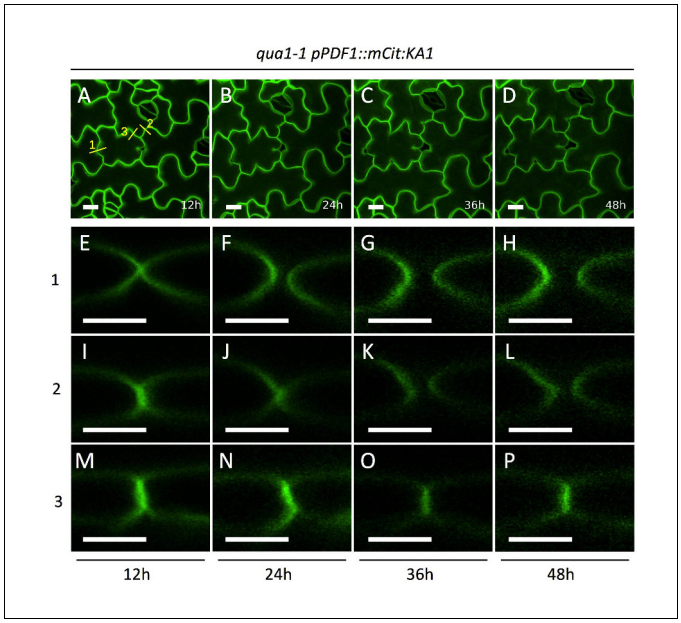

Figure 1—figure supplement 3. Dynamics of cell separation in *qua1-1* cotyledon epidermis. (**A–D**) Z-projections (maximal intensity) of confocal stacks from representative, *qua1-1 pPDF1::mCit:KA1* cotyledons pavements cells at t = 12 hr (**A**), t = 24 hr (**B**), t = 36 hr (**C**) and t = 48 hr (**D**) corresponding to ***Video 2***. (**E–P**) Orthogonal section through the original Z-Stacks, corresponding to panel A yellow line #1 (**E–H**), #2 (**I–L**) and #3 (**M–P**) at t = 12 hr (**E, I, M**), t = 24 hr (**F, J, N**), t = 36 hr (**G, K, O**) and t = 48 hr (**H, L, P**). Scale bars are 10 µm in A-D and 5 µm in E-P.

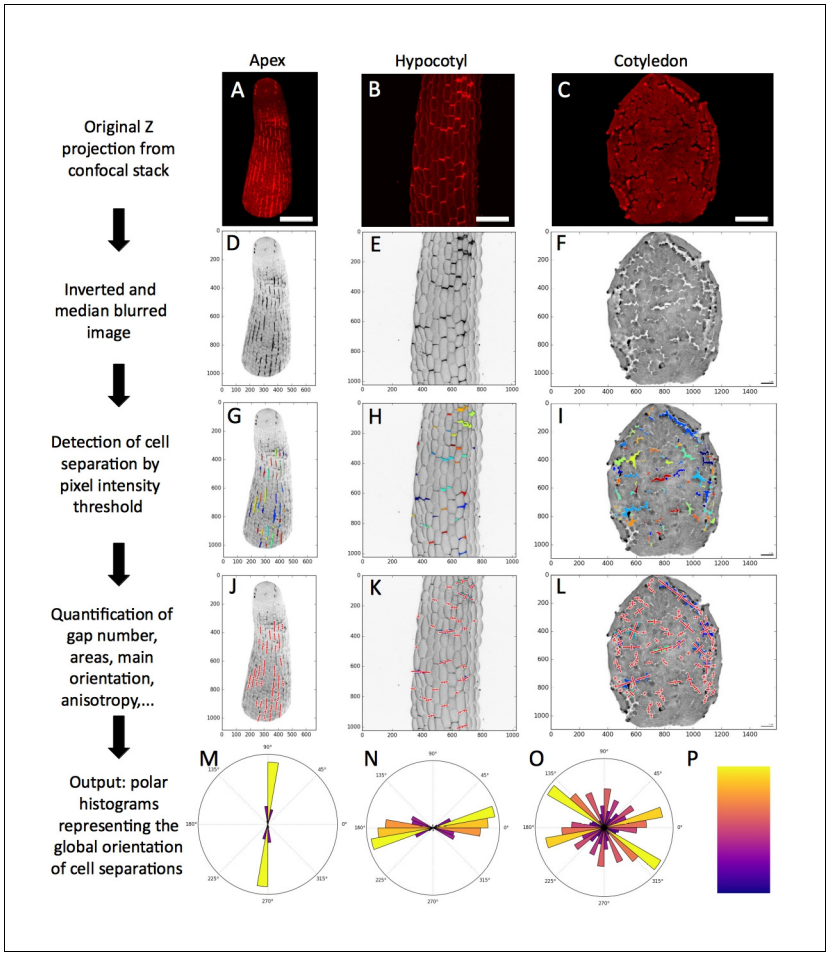

Figure 1—figure supplement 4. A semi automated cell separation image analysis pipeline. (**A–C**) Original maximal intensity Z-projections from confocal stacks of a *qua1-1* mutant shoot apex (**A**), light-grown hypocotyl (**B**) and cotyledon (**C**). (**D–F**) Images are preprocessed in imageJ: a median blur with a radius of 3 is applied to reduce the noise and ease the segmentation, contrasts are enhanced, and the threshold tool is used to determine the appropriate threshold for segmentation in the pipeline. (**G–O**) The python script of the pipeline is then run. (**G–I**) The images are segmented based on the threshold previously defined, and using the 'label' functions of the scipy.ndimage python library. When there are clear gaps between cells (like in cotyledons), the threshold is used to segment areas of low intensity pixels (**I**). In the case of bright PI stripes appearing between the cells (like in the shoot apex or the light grown hypocotyl), the threshold is used to segment areas of high intensity pixels (**G, H**). Labels (i.e. identified gap areas) that are too large (background), or too small (remaining noise), are removed. (**J–L**) The labels features are quantified: pixels coordinates, label center, label area in pixel and μm^2, label covariance matrix, eigen vector and eigen value based on the covariance matrix of the label (principal component analysis of the label), label anisotropy (ratio of the principal component, the first eigen value and the second component, the orthogonal eigen value) and the principal orientation of the label (angle in degree ranging from 0° to 180° based on the principal component eigen vector). These characteristics are calculated using functions from the NumPy python library. The resulting vectors are mapped on the image (Red crosses). For better visualization, the eigen vector that are mapped on the images are multiplied by a factor two and by the square root of the corresponding eigen value (see below). (**M–O**) A polar histogram of the principal angles for each sample, as well as for all the samples in one condition (***Figures 3*** and ***4***) is produced. A weight corresponding to the square root of the principal eigen value for each plotted angle is added to normalize the angle value by its relative importance. (**P**) Color map used in the polar histograms representing the relative number of angles binned in each histogram bar (independently of their weight) where yellow is high and purple is low. Scale bars (**A, B**): 50 µm. Scale bar (**C**), 100 µm.

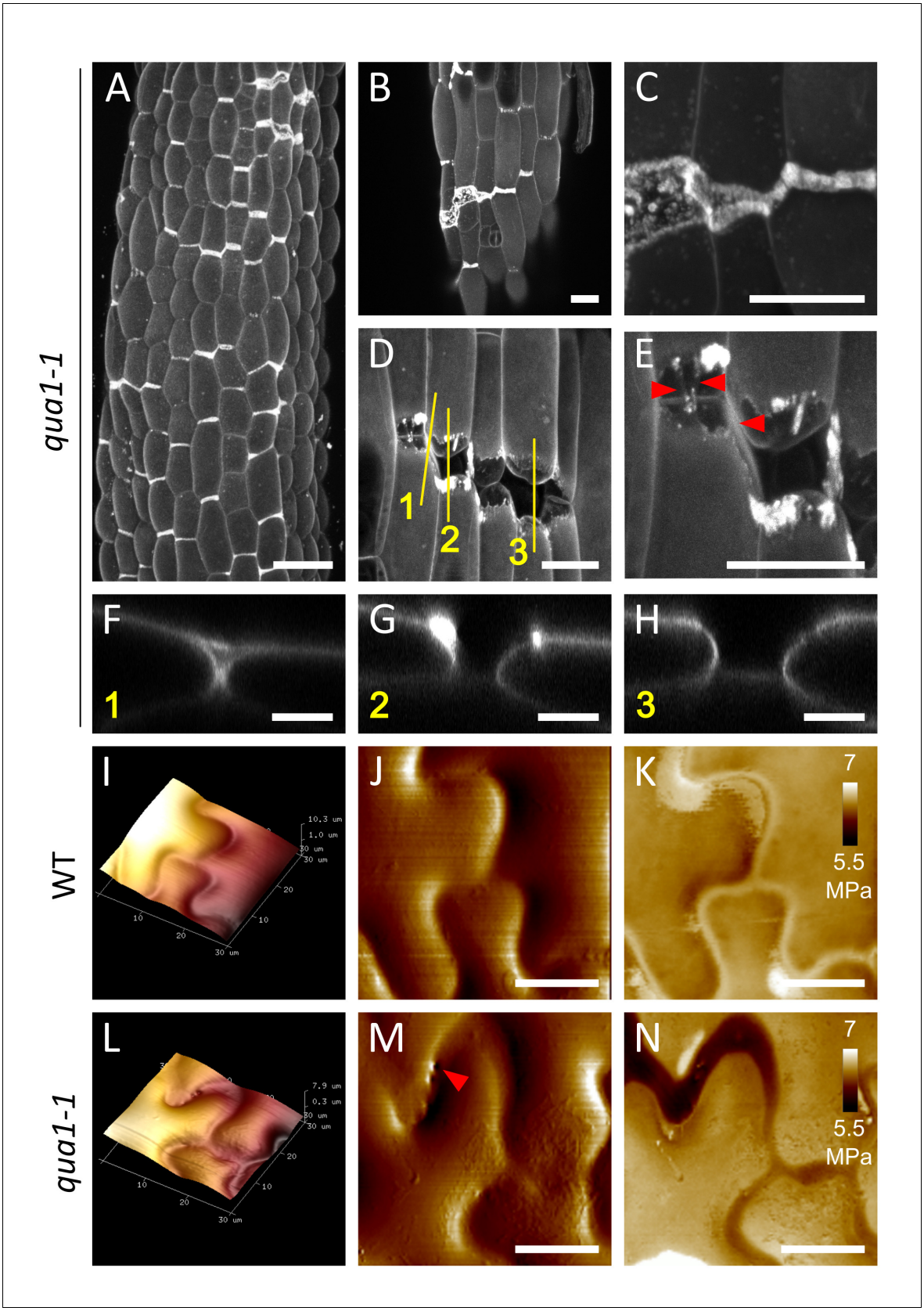

Figure 1—figure supplement 5. Close-ups of cell-cell adhesion defects in *qua1-1*. (**A–E**) Z-projections (maximal intensity) of confocal stacks from propidium iodide stained light-grown *qua1-1* hypocotyls grown on 2.5% agar. Panel A is reproduced from ***Figure 3K***, for ease of reading. Panels C and

Figure 1—figure supplement 5 continued on next page

Figure 1—figure supplement 5 continued

E are close-ups of panels B and D respectively. Panels F, G and H are orthogonal views through the original Z stack of the image in panel D and corresponding respectively to the yellow lines 1, 2 and 3. Panels B and C show a rather small crack that expands to the left, which is the typical type of cracks found on hypocotyls grown on 2.5% agar. Panels D and E show a larger crack with complete separation of some cells, but also some very bright staining in some parts likely remaining from the initial crack. Panel E also reveals the presence of threads (red arrows), likely from the outer wall being pulled apart, consistent with original SEM observations of *qua1-1* gaps (**Bouton et al., 2002**). (**I–N**) Atomic Force Microscopy (AFM) images from 4-day old wild-type (**I–K**) and *qua1-1* (**L–N**) cotyledons. (**I and L**) 3D rendering of the epidermis topography (Height channel). Lighter regions are more elevated than darker ones. (**J and M**) Topography map (Peak Force Error channel). (**K and N**) Stiffness map of the outer walls (LogDMTModulus channel), ranging from 5.5 MPa (black) to 7 MPa (white). While for the wild type, the cell to cell connections form a clearly defined 'valley' and are stiffer, in *qua1-1* these regions are flatter and softer. The red arrow in panel M points to holes in the flat and soft region, suggesting that this zone may be a sheet of outer wall detached from the underlying cells, consistent with panels E and F, and the original SEM observations of *qua1-1* gaps (**Bouton et al., 2002**). Scale bars, (**A**), 50 µm; (**B–E**), 20 µm; (**F–H, J, K, M, N**), 10 µm.

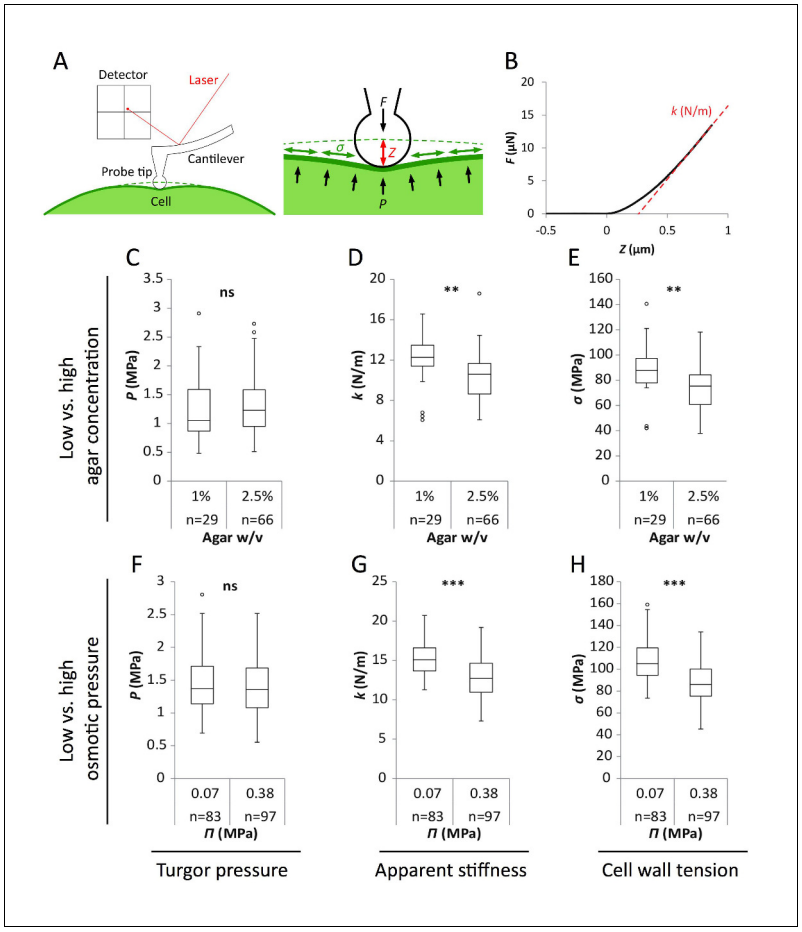

Figure 2. Reduced water potential in growth medium causes decrease in pavement cell stiffness and cell wall tension, not turgor pressure. (**A**) Schematic representation of AFM nano-indentation principle of measurements. *F*, indentation force; *Z*, indentation depth; *P*, turgor pressure; σ, cell wall tension. (**B**) Example of a typical AFM force curve (black line) and linear fit at deep indentation (red dotted line, 75 ~ 99% of maximum force) which depicts apparent stiffness *k*. (**C–H**) Box plots of the turgor pressure *P* (**C,F**), apparent stiffness *k* (**D,G**) and cell wall tension σ (**E,H**) of cotyledon pavement cells grown on medium with differential agar concentration (1% and 2.5% w/v) (**C–E**) or osmotic pressure Π (0.07 and 0.38 MPa) (**F–H**). Circles indicate Tukey's outliers. Student's *t*-test, ** indicates p-value<0.01; ***, p-value<0.001; ns, not significant; *n*, number of measured cells.

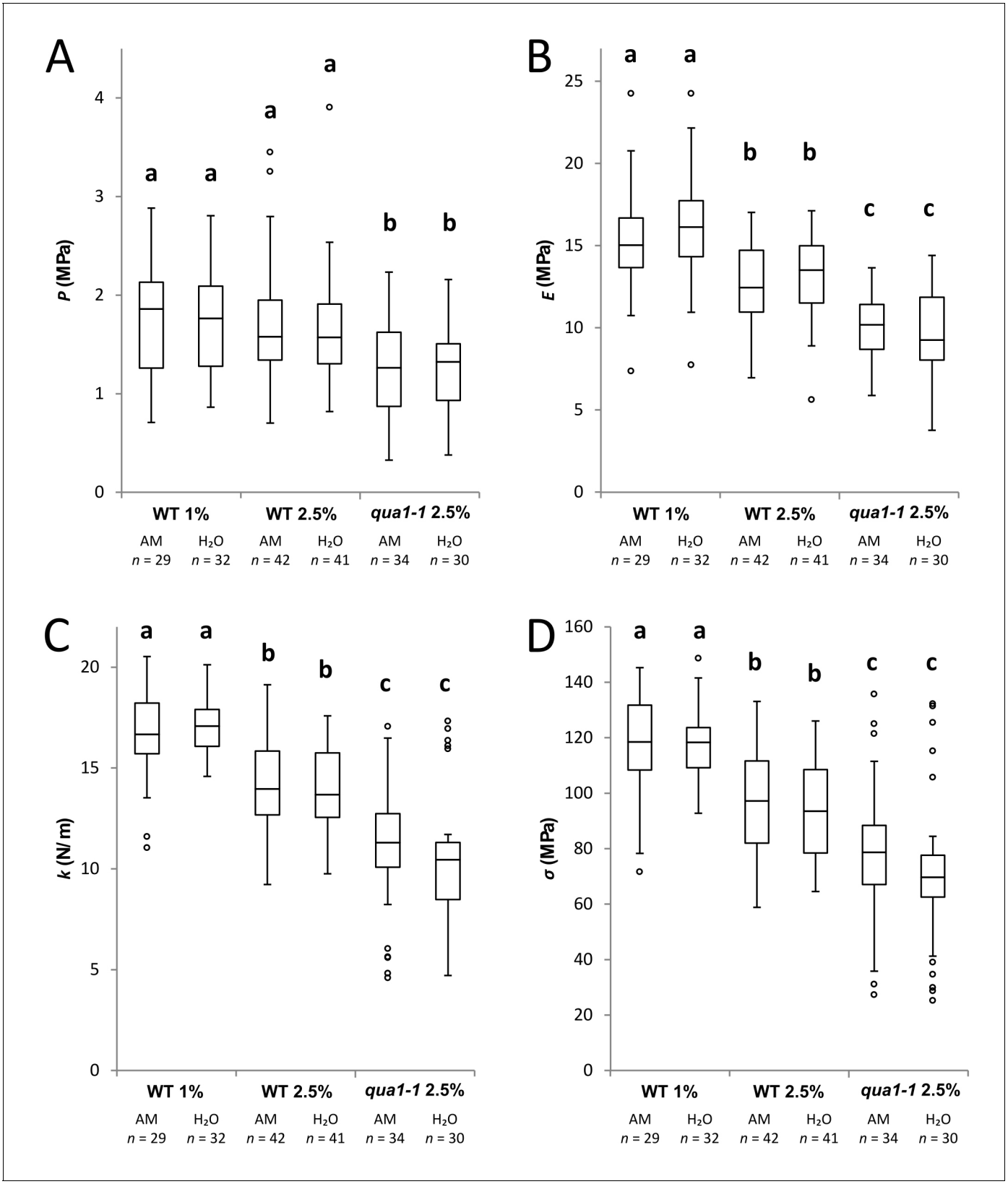

Figure 2—figure supplement 1. Controls for AFM measurements. Box plots of the turgor pressure *P* (**A**), elastic modulus E (**B**), apparent stiffness *k* (**C**) and cell wall tension σ (**D**) of the outer periclinal wall in WT and *qua1-1* cotyledon pavement cells grown on medium with different agar concentration (1% and 2.5% w/v). After mounting, the samples were first immersed in liquid Arabidopsis medium (AM, with an osmotic pressure of 0.07 MPa) and

Figure 2—figure supplement 1 continued on next page

Figure 2—figure supplement 1 continued

measured; the Arabidopsis medium was then removed and replaced by pure water (H_2O) and the same sample was measured again. For each immersion, the duration of the experiment, from sample preparation to the end of AFM measurement, was about 30 min. The two immersion solutions had no impact on the measured properties in that time window. Measurements were done by pair (AM then water immersion) on six samples. Statistical significance was tested by Student's t-test. a b c are significantly different groups. Within group p-value>0.05. Between groups p-value<0.001. Circles indicate Tukey's outliers; *n*, number of measured cells.

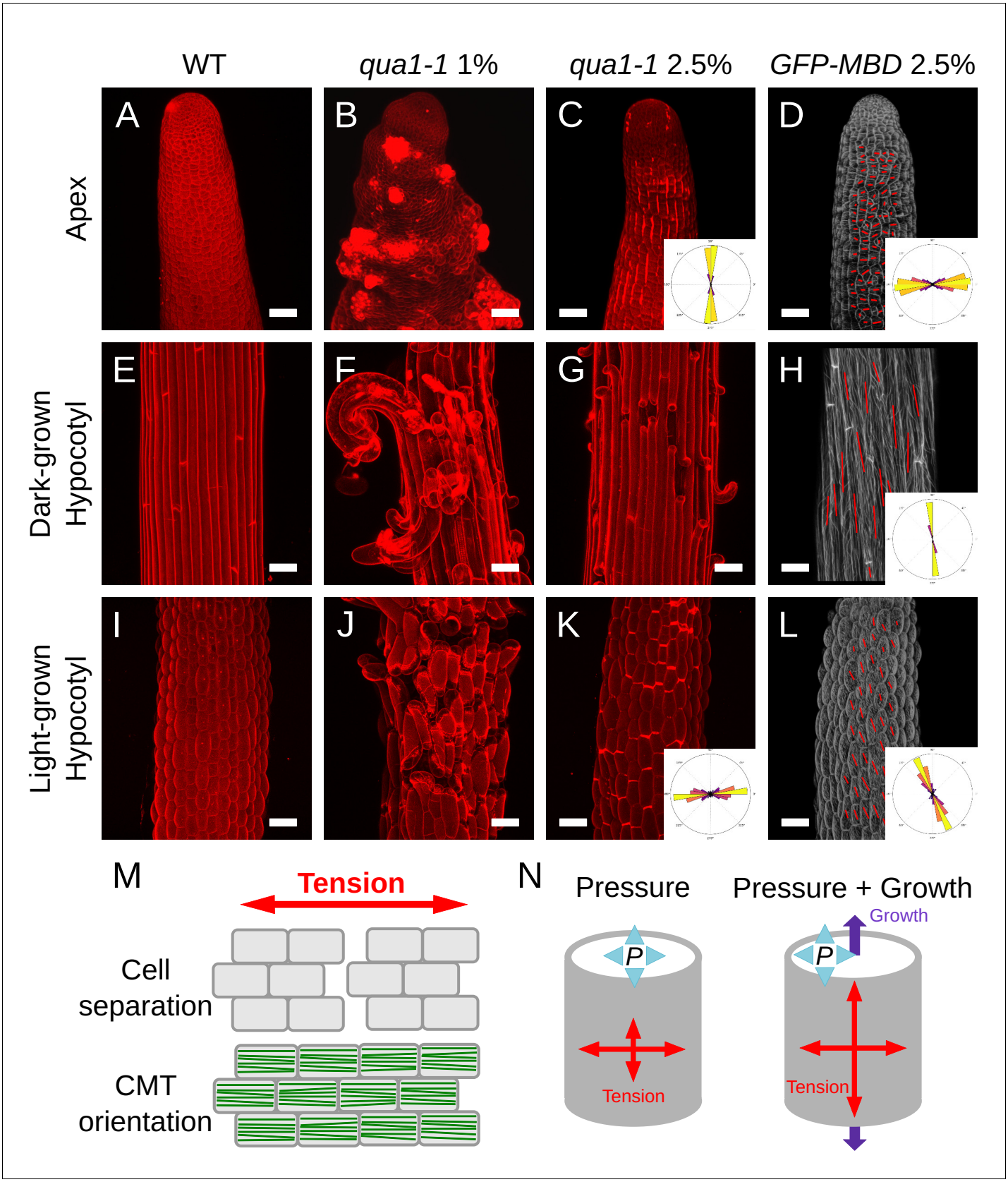

Figure 3. Both shape derived and growth derived tensile stress contribute to the tensile stress pattern in cylindrical organs. (**A–C, E–G and I–K**) Z-projections (maximal intensity) of confocal stacks from representative, propidium iodide stained, shoot apex (**A–C**), dark-grown hypocotyl (**E–G**) and

Figure 3 continued on next page

Figure 3 continued

light-grown hypocotyl (**I–K**), from wild type grown on 1% agar medium (**A, E and I**), *qua1-1* grown on 1% agar medium (**B, F and J**) and *qua1-1* grown on 2.5% agar (**C, G and K**). (**D, H and L**) Surface signal extracted from confocal stacks, of representative, *GFP-MBD*, shoot apex (**D**), dark-grown hypocotyl (**H**) and light-grown hypocotyl (**L**) grown on 2.5% agar medium. Red lines are the output of the FibrilTool macro, giving a visual representation of the cortical microtubule arrays orientation and anisotropy. The polar histograms in C and K show the global distribution of cell separation orientation in 8 samples from three biological replicates. The polar histograms in D, H and L show the distribution of microtubule array orientations for 12 samples. (**M**) Schematic representation of the relationship between tensile stress and cell separation in the *qua1-1* mutant, and cortical microtubule array organization in the wild type. An horizontal tension will pull the cells apart and create a vertical gap between the cells, perpendicular to the tensile stress pattern, while the microtubules in a wild type context will align horizontally, parallel to the tensile stress pattern. (**N**) Schematic representation of the effect of pressure and growth derived stress on the resulting tensile stress pattern in a cylinder. Shape derived stress is caused by the global turgor pressure of the tissue that puts the epidermis under tension. For a cylindrical shape, this results in a tension twice as high in the transverse direction than in the longitudinal direction (***Beer and Johnston, 1992***). Unidirectional growth driven by the inner tissue layers can also put the outer wall of the epidermis under tension, prescribing maximal tensile stress parallel to the growth direction. Scale bars, 50 µm.

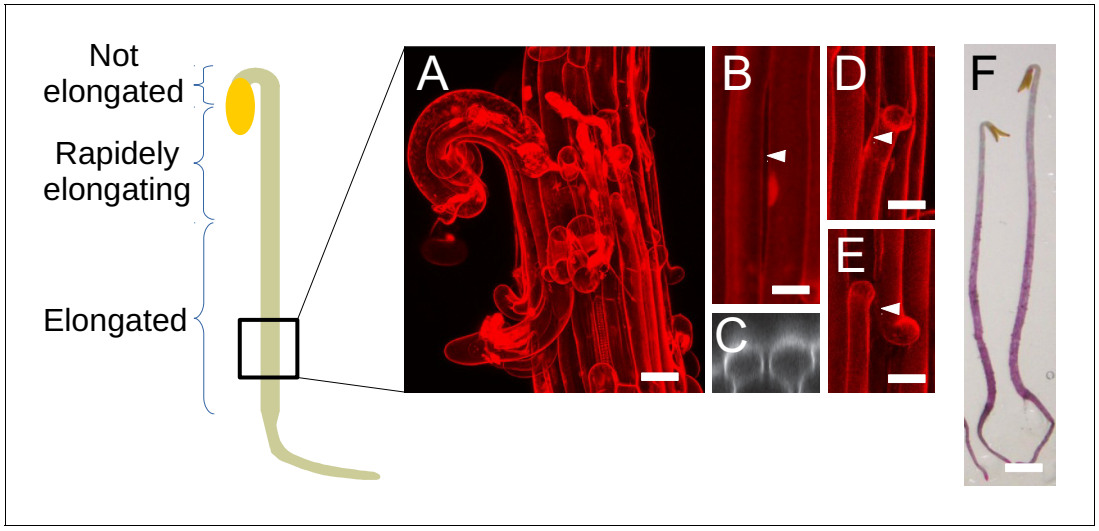

Figure 3—figure supplement 1. Dark-grown hypocotyl growth and cell separation patterns. Schematic representation of a dark-grown hypocotyl, and annotated growth pattern. The square at the bottom represent the relative position where images were taken on dark-grown hypocotyl, in *qua1-1* for cell separation as well as for *GFP-MBD* cortical microtubule orientation. (**A**) Panel reproduced from ***Figure 3F***, for ease of reading. (**B**) An example of longitudinal cell separation in a dark-grown hypocotyl. (**C**) Orthogonal view of the cell separation shown in panel *B*. White arrowhead indicates the site of separation. (**D and E**) Examples of longitudinal cell separations associated with at least one transverse cell separation. White arrowheads indicate the site of separation. (**F**) Stereo microscope picture of *qua1-1* dark-grown hypocotyl stained with ruthenium red (a dye that stains unesterified pectins; ***Steeling, 1970***), and thus stains the cell wall only if the cuticle is cracked) revealing more frequent and larger cell separation at the rootward part of the hypocotyl. Scale bar (**A**), 50 µm. Scale bars (**B–E**), 20 µm. Scale bar (**F**), 1 mm.

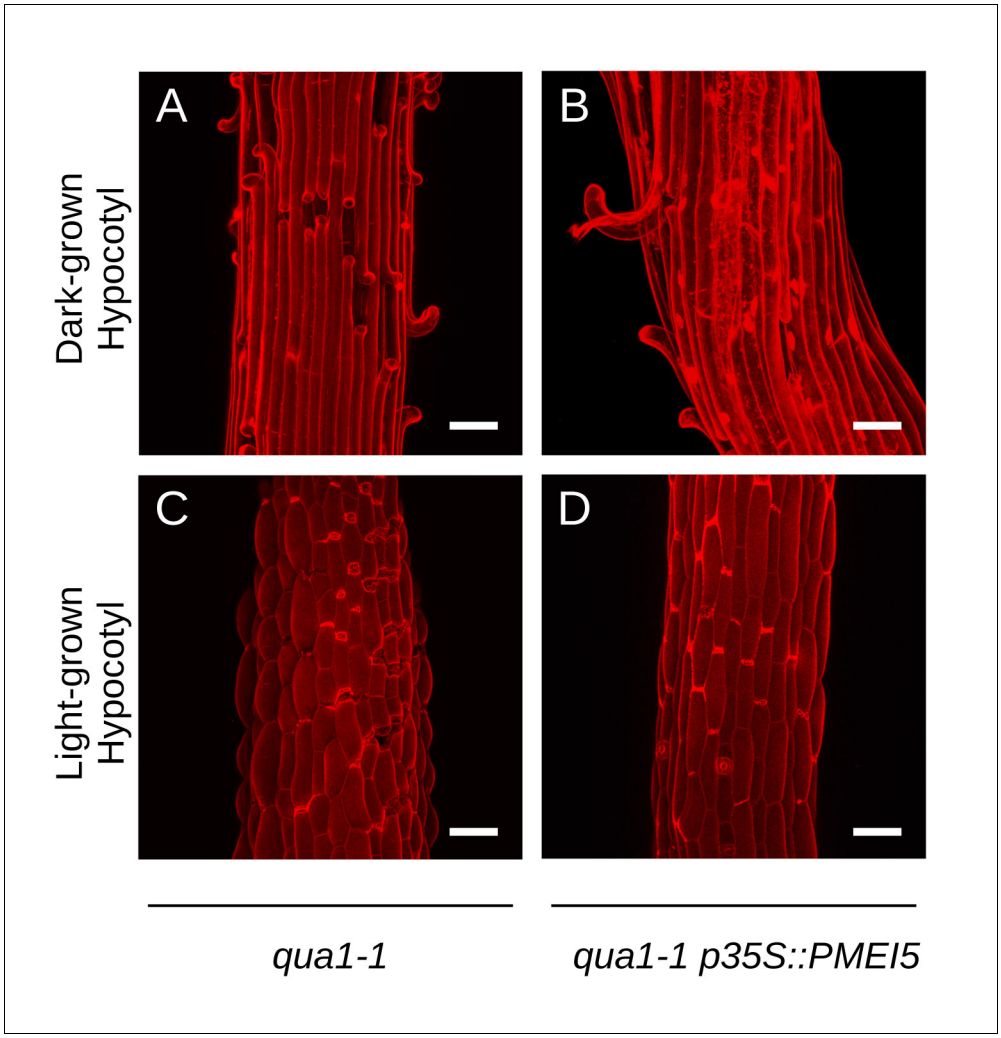

Figure 3—figure supplement 2. Reduction of heterogeneity in pectin esterification in *qua1-1* has no major impact on cell separation patterns. (**A–D**) Z-projections (maximal intensity) of confocal stacks from representative, propidium iodide stained, dark-grown hypocotyl (**A, B**) and light-grown hypocotyl (**C, D**), from *qua1-1* (**A, C**) and *qua1-1 p35S::PMEI5* (**B, D**) grown on 2.5% agar. Panel A is reproduced from ***Figure 3G***, for ease of reading. Scale bars, 50 μm.

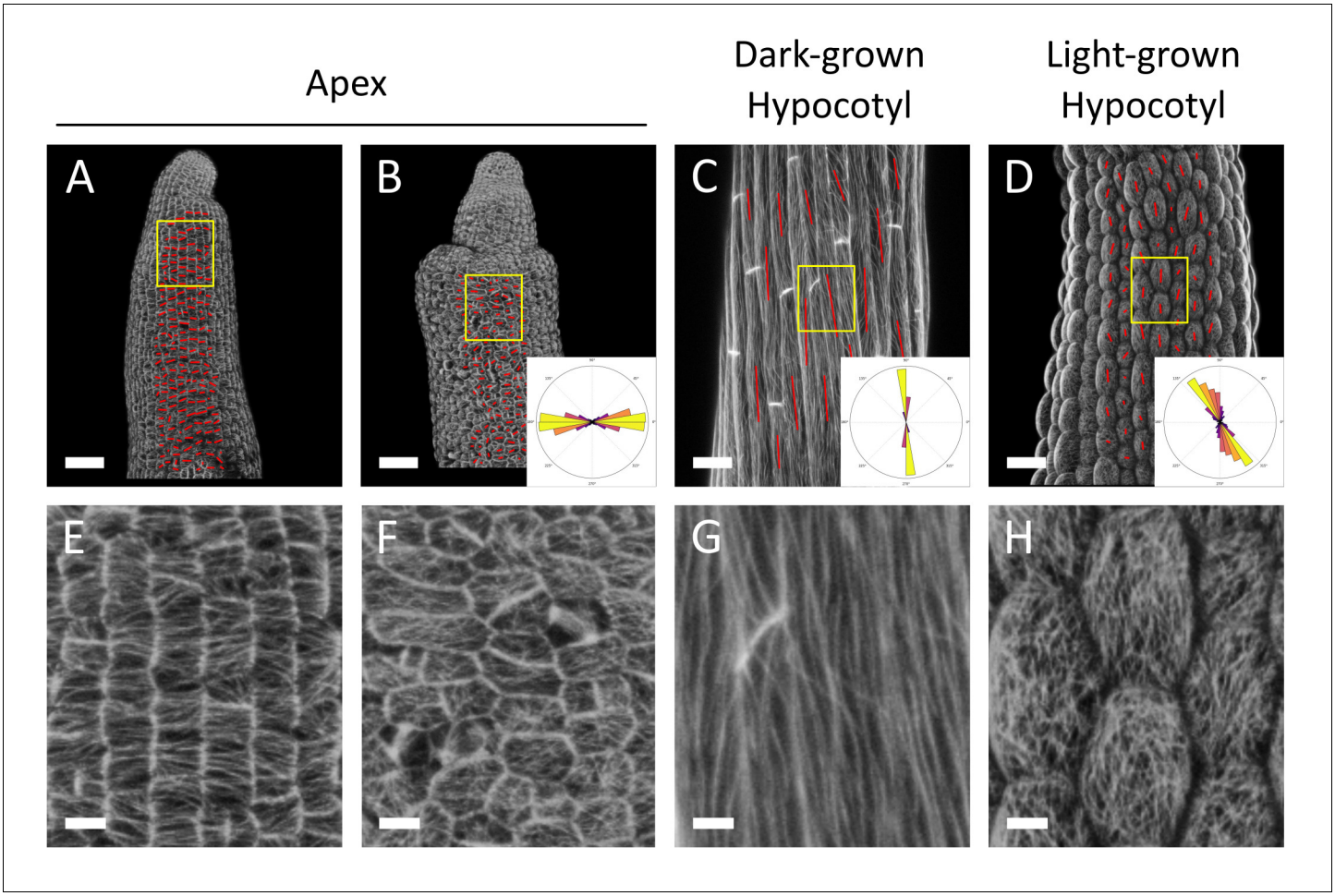

Figure 3—figure supplement 3. CMT behavior in *GFP-MBD* plants grown on 1% agar. Surface signal extracted from confocal stacks of two representative *GFP-MBD* stem apices (**A,B**), a representative dark-grown hypocotyl (**C**) and a representative light-grown hypocotyl (**D**) grown on 1% agar. Red lines are the output of the FibrilTool macro, giving a visual representation of the CMT array orientation and anisotropy. The polar histograms in B, C and D show the distribution of microtubule array orientations for 12 samples (**A,B**) or 10 samples (**C and D**). Note that NPA-induced naked stems exhibited bumps more frequently on 1% agar medium (as shown in panel B), than on 2.5% agar medium (see ***Figure 3D***), resulting in increased noise in CMT orientations. Scale bars, (**A–D**), 50 µm; (**E–H**), 10 µm.

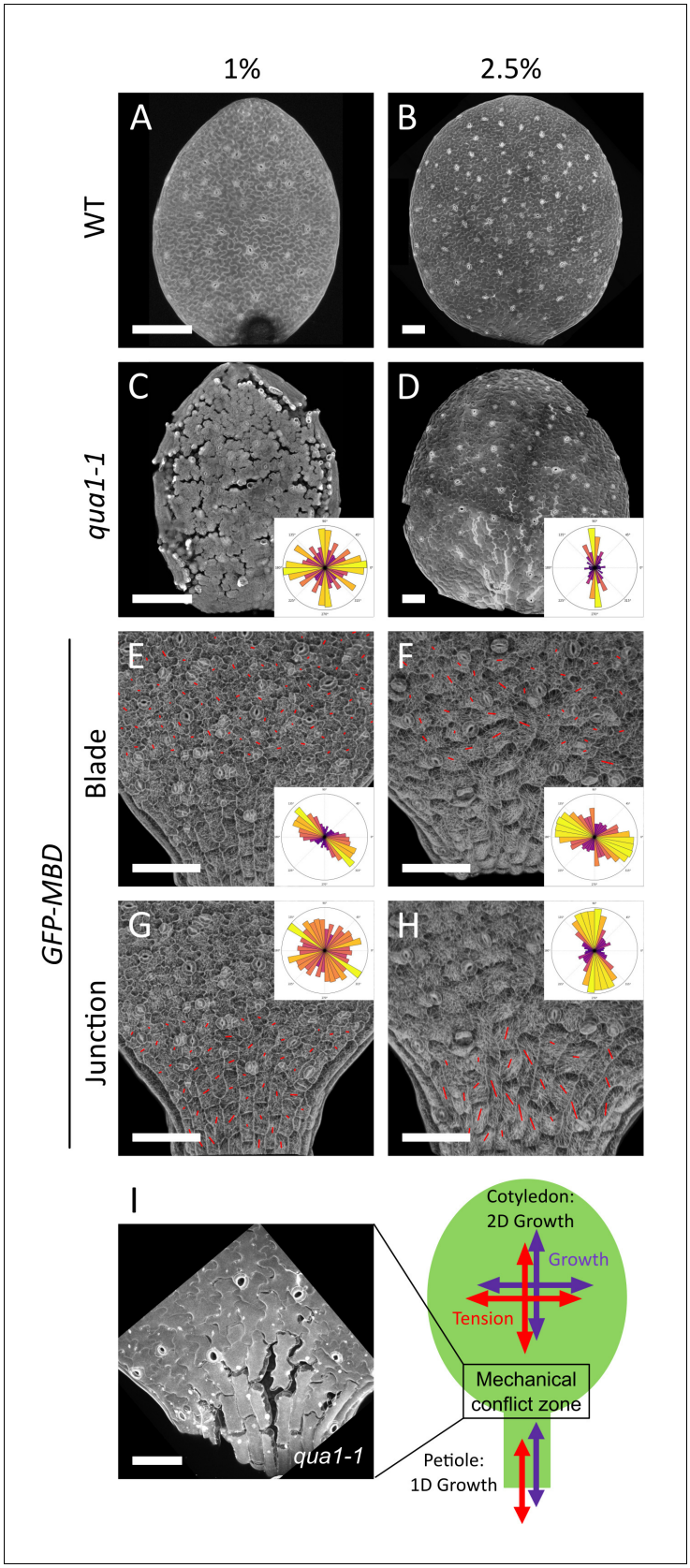

Figure 4. A mechanical conflict at the petiole-blade junction in cotyledons. (**A–D**) Z-projections (maximal intensity) of confocal stacks from representative, propidium iodide stained, 3-day (**A**) or 5-day (**B**) old WT cotyledons and 3-

Figure 4 continued on next page

Figure 4 continued

day (**C**) or 5-day (**D**) old *qua1-1* cotyledons grown on 1% (**A, C**) and 2.5% (**B,D**) agar medium. (**E–H**) Surface signal extracted from confocal stacks, of representative *GFP-MBD* cotyledons grown on 1% (E,G; n = 12 cotyledons) and 2.5% (F,H; n = 13 cotyledons) agar medium. Red lines are the output of the FibrilTool macro for the blade region (E (n = 898 cells), F (n = 639 cells)) and petiole-blade junction (G (n = 550 cells), H (n = 425 cells)). The polar histograms in C and D show the global distribution of cell separation orientation in *qua1-1* cotyledons (respectively 12 and 8 samples from three biological replicates); the polar histograms in E-H show the distribution of microtubule array orientations for 12 samples. (**I**) Schematic representation of the effect of differential growth from the cotyledon and the petiole resulting in a mechanical conflict at the junction with higher tensile stress. The close-up image is extracted from a petiole-blade junction in the *qua1-1* mutant. Scale bars, 100 µm.

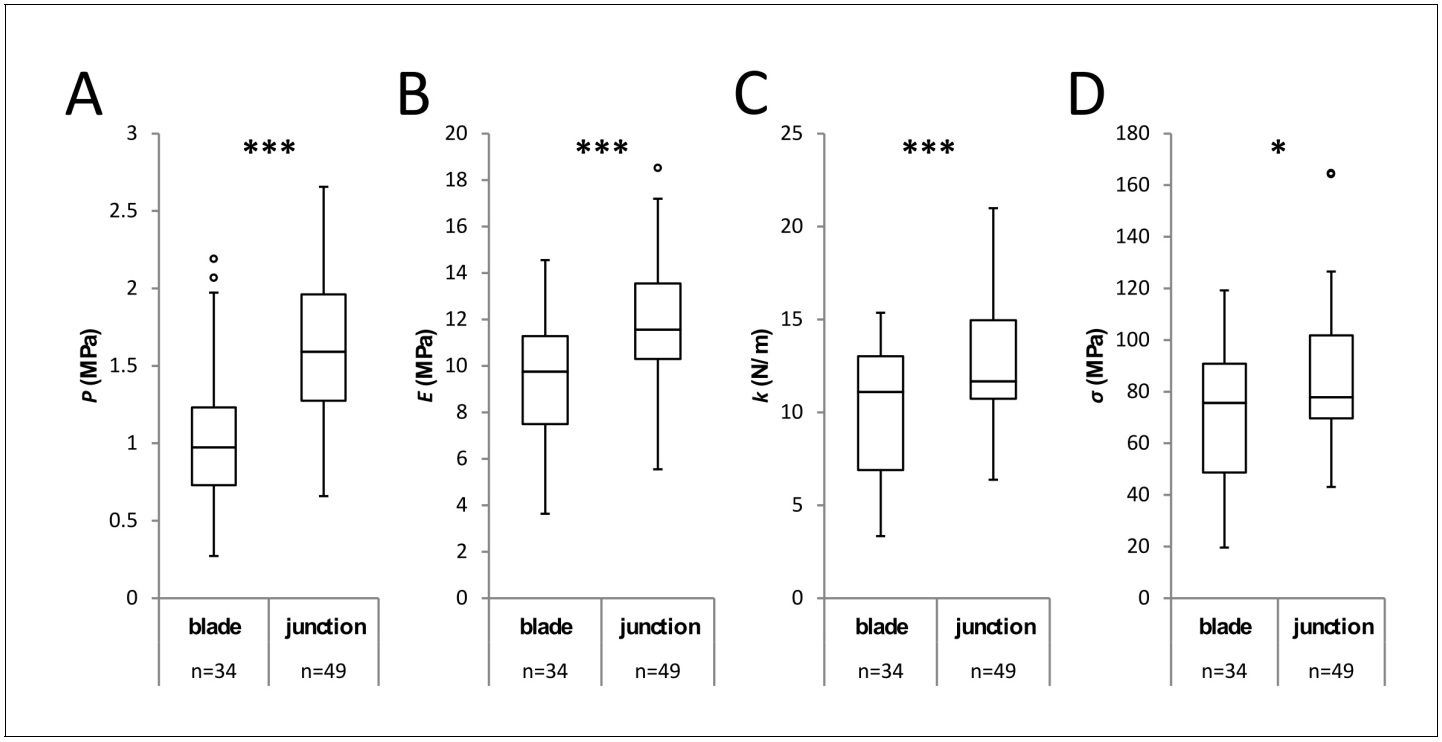

Figure 4—figure supplement 1. Mechanical assessment of the cotyledon's petiole-blade junction by AFM. Box plots of the turgor pressure *P* (**A**), cell wall elastic modulus *E* (**B**), apparent stiffness *k* (**C**) and cell wall tension σ (**D**) comparing cells at the blade and at the petiole-blade junction (see ***Figure 4***) from wild-type seedlings grown on 2.5% agar medium. Measurements on each domain were done pairwise on 10 cotyledons. Circles indicate Tukey's outliers. Student's t-test, *** indicates p-value<0.001; *, p-value<0.05; n, number of measured cells.

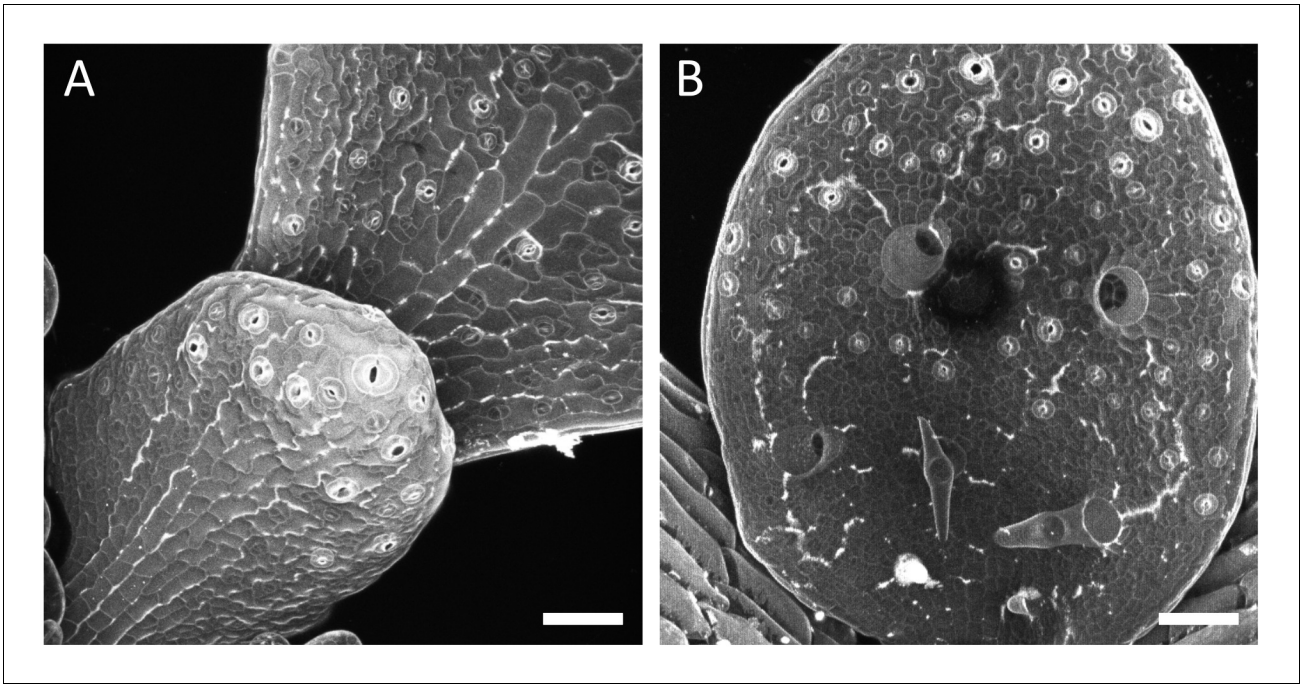

Figure 4—figure supplement 2. Gaping pattern in the third leaf of *qua1-1* seedlings. (**A–B**) Z-projections (maximal intensity) of confocal stacks from, propidium iodide stained young leaves from *qua1-1* seedlings grown on 1% agar medium. In panel A, the top right corner leaf is the third leaf, and the bottom left corner leaf is the fourth leaf. Leaf in B is the third leaf. Note the presence of longitudinal cracks at the base of the leaves and radial cracks around trichomes. Scale bars, 50 μm.

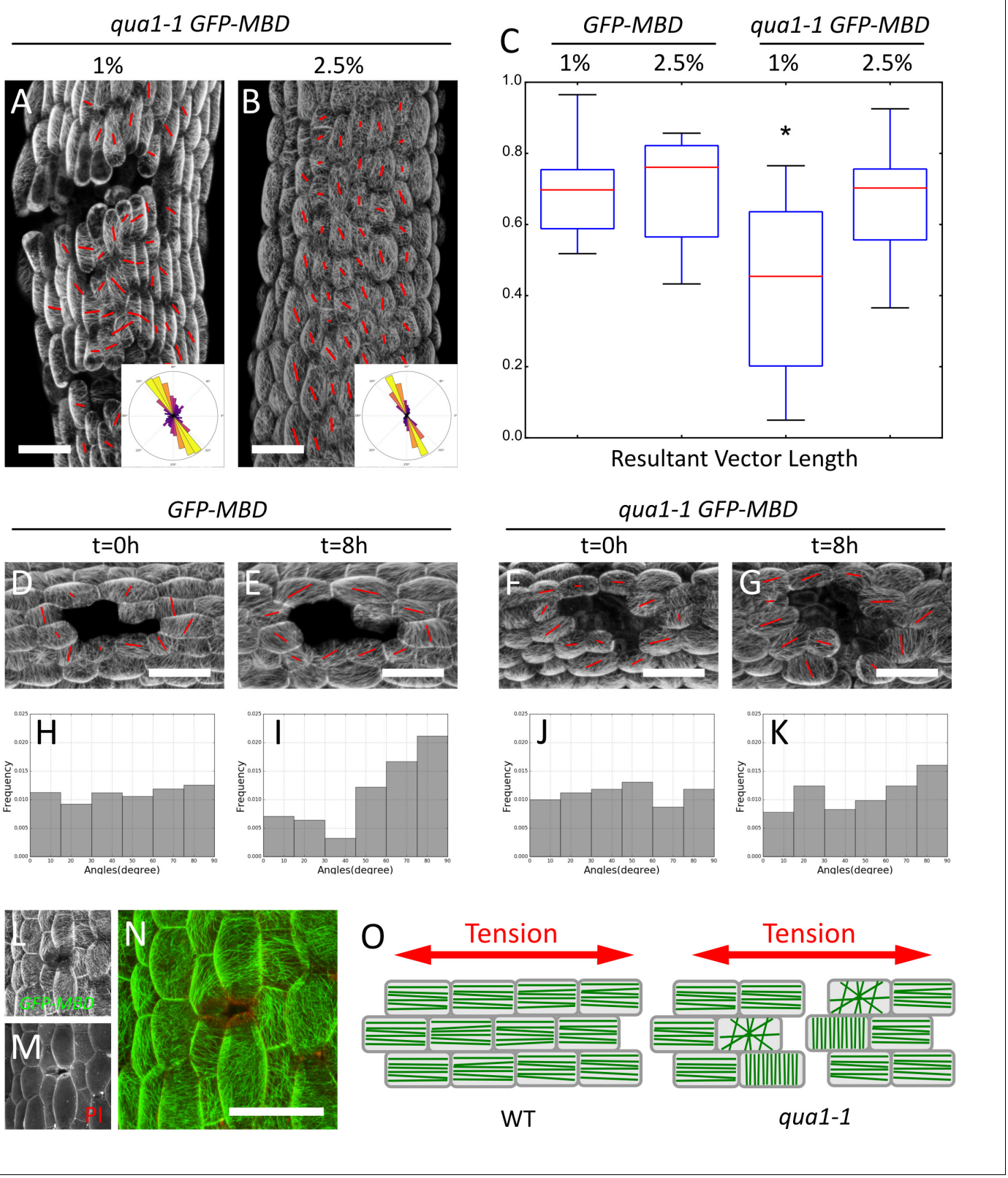

Figure 5. Epidermis continuity is required for tensile stress propagation and supracellular alignment of cortical microtubules. (**A**,**B**) Surface signal extracted from confocal stacks of representative *qua1-1 GFP-MBD* light-grown hypocotyls. Red lines in A and B are the output of the FibrilTool macro.

Figure 5 continued on next page

Figure 5 continued

Cell separation affects cortical microtubule arrays cell to cell coordination across the tissue as compared to ***Figure 3L***. The polar histograms in A and B show the global distribution of microtubule array orientations in 15 (**A**) and 16 (**B**) samples from three biological replicates. (**C**) Box plot of the resultant vector length revealing less consistent CMT alignment in *qua1-1* hypocotyls grown on 1% agar medium, and a rescue of this defect in *qua1-1* hypocotyls grown on 2.5% agar medium. (**D–K**) Ablation experiment showing the reorganisation of CMT in response to the modified stress pattern in *GFP-MBD* (**D and E**) and *qua1-1 GFP-MBD* (**F and G**), at t = 0 hr after the ablation (**D and F**) and t = 8 hr after the ablation (**E and G**) (10 samples from three biological replicates for each condition). (**H–K**) Histograms of the distributions of CMT array angles relative to the ablation site, and corresponding to panels D-G. (**L–N**) Local impact of a cell-cell adhesion defect in *qua1-1 GFP-MBD*: CMTs align along the local maximum of tension around the gap. (**L**) *GFP-MBD* signal, (**M**) Propidium Iodide signal, (**N**) overlay. (**O**) Schematic representation of the effect of cell separation in the *qua1-1* mutant on cortical microtubule array organization. In the wild type, tension is propagated across the tissue in the epidermis, leading to consistent CMT array alignments in the tissue. In contrast, in *qua1*, the mechanical discontinuity of the epidermis hinders the normal propagation of the tension across the tissue and locally affects the pattern of stress, leading to less pronounced CMT array alignments in the tissue. Scale bars, 50 μm.

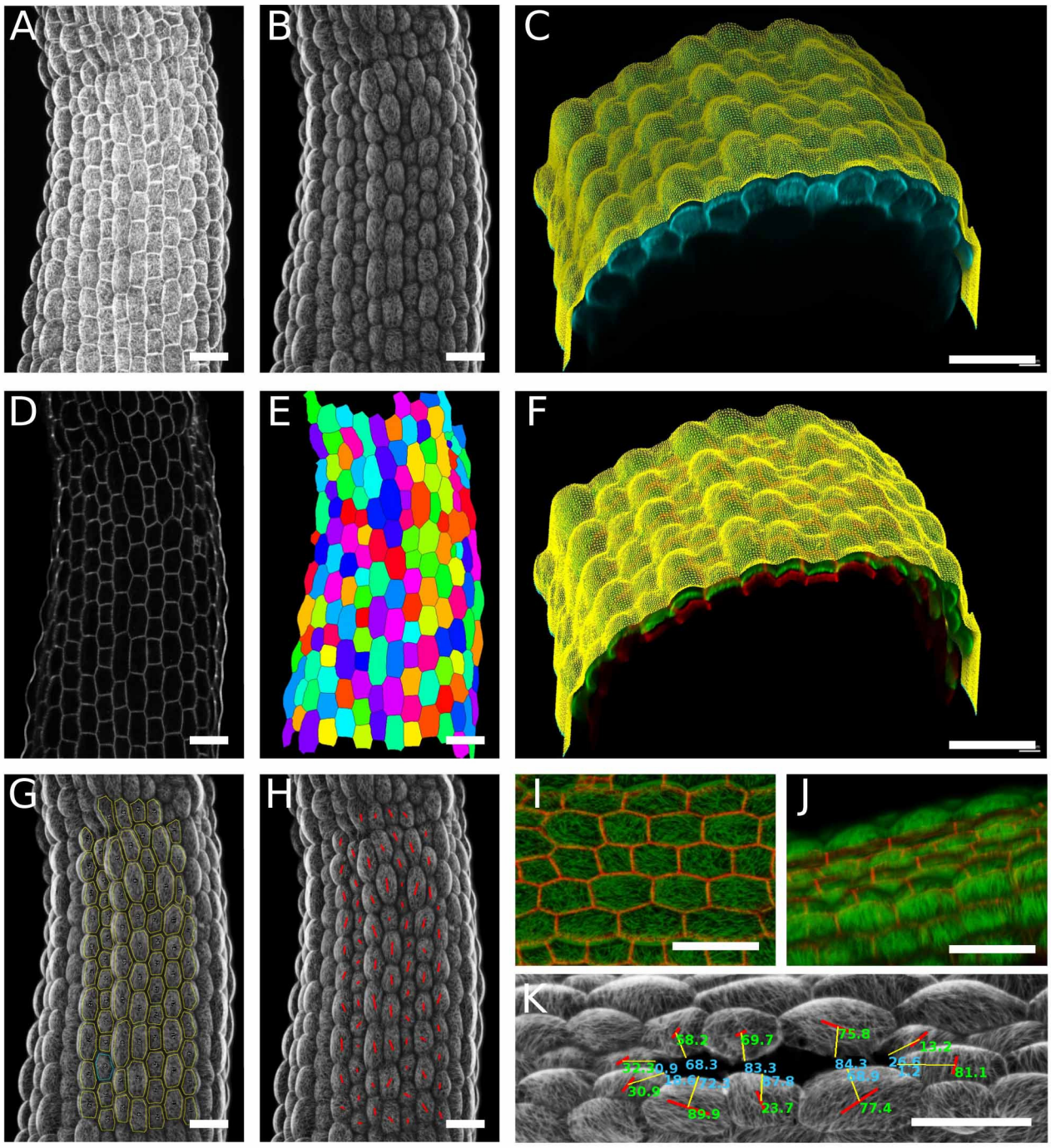

Figure 5—figure supplement 1. Surface signal extraction and semi-automated CMT array quantification. (**A**) Original max intensity Z-projections from a confocal stack of a *GFP-MBD* light-grown hypocotyl. (**B**) The original stack is cropped at a distance of 0 to 8 µm from the surface in MGX, to extract the outer epidermal CMT signal. (**C**) Original confocal stack (cyan) and surface's mesh created in MGX (yellow). (**D**) The original stack is cropped at a distance of 10 to 14 µm from the surface in MGX, to obtain the cells contour only. (**E**) The cell contour image is then used to segment the cells using the morphological segmentation tool from the morpholibJ library (***Legland et al., 2016***). Clear and properly segmented cell contours were obtained, the image was inverted, and the cell edges dilated. (**F**) The original stack after cropping in MGX with the outer signal (CMTs, in green) and inner signal (cell contours, in red). (**G**) Using the 'analyze particle tool' in ImageJ we created a list of ROIs (in yellow). (**H**) For each cell, the principal orientations and anisotropy of CMT arrays were quantified using an automated version of the FibrilTool macro (***Boudaoud et al., 2014***) based on the list of ROIs and

Figure 5—figure supplement 1 continued on next page

Figure 5—figure supplement 1 continued

the CMT surface signal image. (**I**) Top view of cell contours (red) and surface signal (green). (**J**) Side view of the sample shown in panel I; CMT orientation and anisotropies were only calculated based on top-view images. (**K**) In ablation experiments, ROIs were manually drawn for each cell surrounding the ablation and the CMT array orientation and anisotropy were quantified with FibrilTool. In addition, cell positions were measured as an angle relative to the ablation site. To do so, a line (yellow lines) was drawn from the center of the cell (middle of the FibrilTool red segment) to the middle of innermost anticlinal wall towards the ablation. The angle of this line (number in light blue) describes the position of the cell relative to the ablation and the hypocotyl axis. For instance, if this angle is 0°, this means that cell is either positioned rootward or shootward relative to the ablation site. The acute angle between the yellow line and the angle of the FibrilTool output (red lines) was calculated, giving the angle of CMT orientation relative to the ablation (in green, for example 90° correspond to a CMT array oriented circumferentially around the ablation). Scale bars, 50 μm.

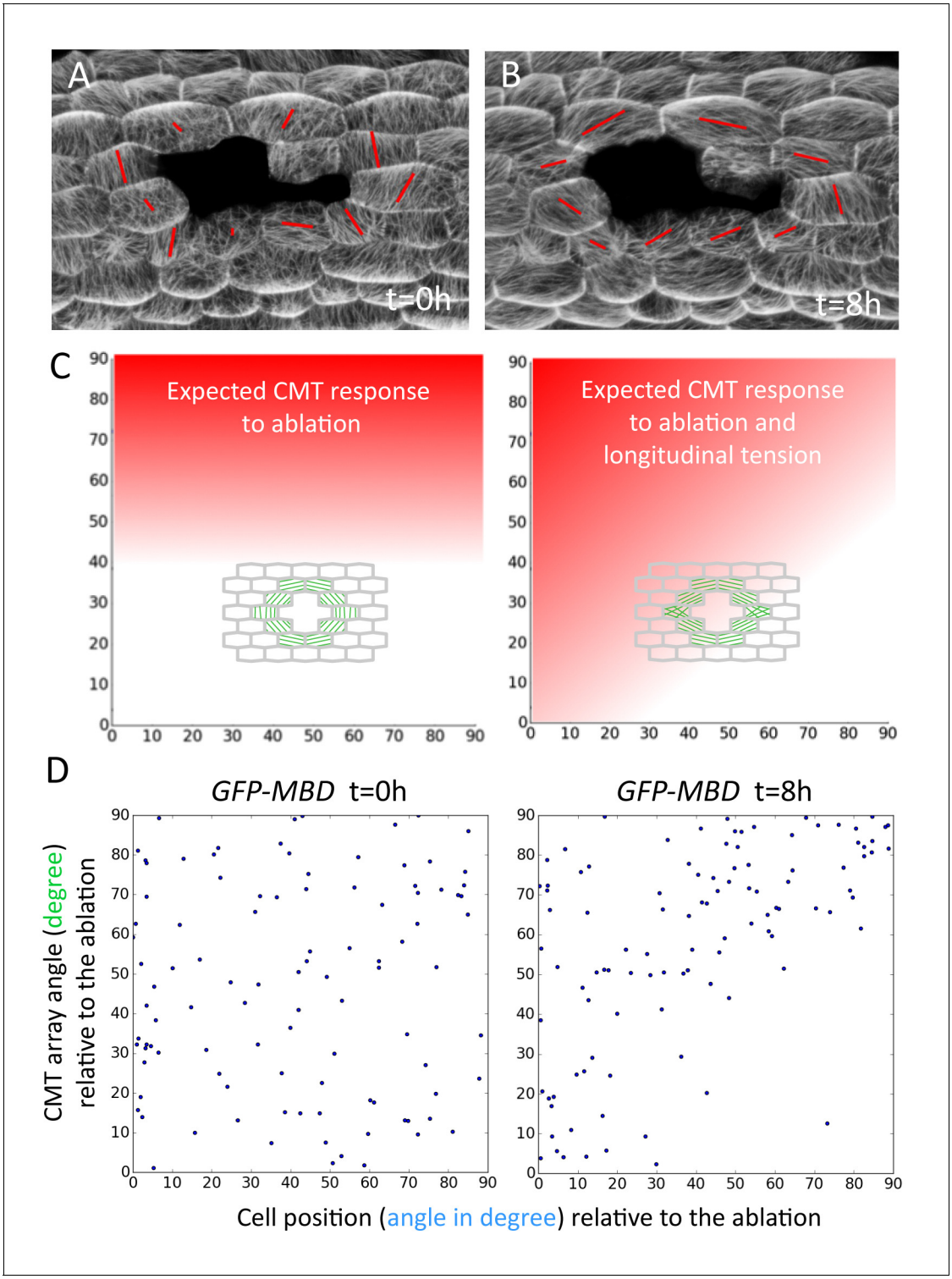

Figure 5—figure supplement 2. Conflict between ablation-derived (circumferential) and growth-derived (longitudinal) tensile stress in the hypocotyl outer epidermal cell wall. (**A, B**) These panels are reproduced from ***Figure 5B and C*** for ease of reading. CMT response at t = 0 hr (**A**) and t = 8 hr after ablation (**B**). (**C**) Predicted distribution of CMT angles according to cell position around an ablation. For instance, 90˚ along the Y axis correspond to a CMT array orienting circumferentially around the ablation; 0˚ along the X axis correspond to cells positioned at the rootward or shootward edges of the ablation site. Left panel: expected distribution of CMT angles and cell positions if the CMT response to ablation dominated. Right panel: expected distribution of CMT angles and cell positions if the CMT respond to both ablation and growth-derived longitudinal stress. The red gradient represents the expected density of points in the area. (**D**) Scatter plot of the actual data distribution at t = 0 hr (left), and t = 8 hr after the ablation (right) (104 cells from 10 samples in three biological replicates).

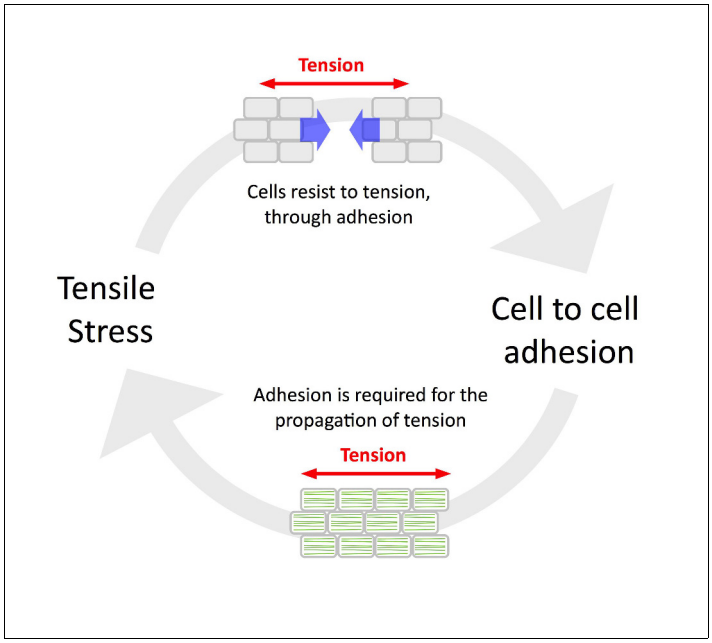

Figure 6. The tension-adhesion feedback loop in plant epidermis. Schematic representation of the relationship between tensile stress and cell to cell adhesion in the epidermis. Tensile stress pulls the cells apart in the *qua1* mutant, while cell to cell adhesion is required to allow the normal propagation of tensile stress in the epidermis, as revealed by the organization of CMT arrays in the *qua1* mutants and the wild type. This paradoxical relationship highlights the importance of epidermis continuity for mechanoperception at the tissue scale.